

# Geomorphological Analysis Using Unpiloted Aircraft Systems, Structure from Motion, and Deep Learning

Zhiang Chen, Tyler R. Scott, Sarah Bearman, Harish Anand,  
Chelsea Scott, J Ramón Arrowsmith, Jnaneshwar Das

**Abstract**—We present a pipeline for geomorphological analysis that uses structure from motion (SfM) and deep learning on close-range aerial imagery to estimate spatial distributions of rock traits (diameter and orientation), along a tectonic fault scarp. Unpiloted aircraft systems (UAS) have enabled acquisition of high-resolution imagery at close range, revolutionizing domains such as infrastructure inspection, precision agriculture, and disaster response. Our pipeline leverages UAS-based imagery to help scientists gain a better understanding of surface processes. Our pipeline uses SfM on aerial imagery to produce a georeferenced orthomosaic with 2 cm/pixel resolution. A human expert annotates rocks on a set of image tiles sampled from the orthomosaic, and these annotations are used to train a deep neural network to detect and segment individual rocks in the whole site. Our pipeline, in effect, automatically extracts semantic information (rock boundaries) on large volumes of unlabeled high-resolution aerial imagery, and subsequent structural analysis and shape descriptors result in estimates of rock diameter and orientation. We present results of our analysis on imagery collected along a fault scarp in the Volcanic Tablelands in eastern California. Although presented in the context of geology, our pipeline can be extended to a variety of morphological analysis tasks in other domains.

## I. INTRODUCTION

Geographic Information Systems (GIS) have helped integrate a wide range of data sources, enabling efficient approaches for geological studies [1]. Traditionally, field surveys have been a gold standard for data collection because of low bias and high tolerance for dealing with ambiguity. However, field surveys are limited by access and time, and may not be as unbiased as previously assumed [2]. Meanwhile, remote sensing for collection of close-range terrestrial data have evolved from traditional methods such as airplanes, balloons, and kites equipped with cameras and LiDARs, to the use of versatile robotic platforms such as Unpiloted Aerial Systems (UAS) or Unpiloted Aerial Vehicles (UAVS). Combining data collection with UAS/UAVs with Structure from Motion (UAS-SfM) is already offering a low-cost solution for rapid mapping of geologic sites, generating data products like digital surface models (DSM), digital elevation models (DEM), and cm-scale orthomosaics.

Our work is motivated by the need for precise large spatial-scale estimation of geologic features that potentially correlate with surface processes around tectonic fault scarps. Currently, analysis of the topographical models produced through SfM largely relies on expert annotation of features of interest (rocks) by hand, followed by estimation of spatial

Authors are affiliated with the School of Earth and Space Exploration, Arizona State University, 781 Terrace Mall, Tempe, AZ 85287, USA

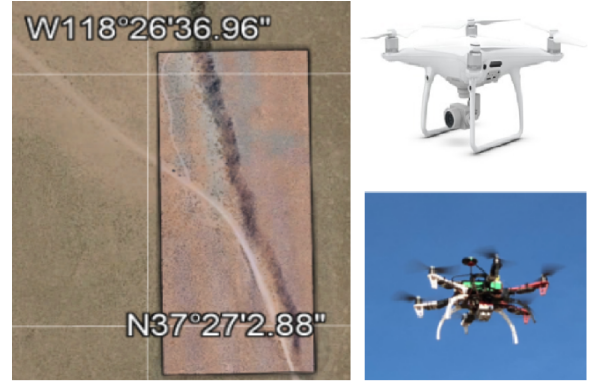


Fig. 1. UAS-SfM generated terrain model overlaid on area of study at a fault scarp in San Andreas, California. Two vehicles used in this study are shown in right inlay.

distributions of rock traits such as major-axis length (diameter) and orientation.

In recent years, deep neural networks have demonstrated unprecedented success in image classification, segmentation, and object detection, leading to extensive application in satellite and airborne image analysis. Close-range UAS imagery provides higher-resolution features that extends the use of deep learning to rock trait estimation over a large range of rock sizes, ranging as low as a few centimeters. Compared to satellite based imaging, UAS imaging has other advantages of low cost, immediacy, agility, and flexibility of choosing cameras.

The key contribution of this paper is a pipeline that combines UAS, SfM and deep learning (UAS-SfM-DL) to produce high-resolution semantic maps of objects such as rocks with wide variation in size and appearance (Fig. 2). The resulting geomorphological analysis techniques discussed can be applied to a range of other tasks such as crop property estimation in precision agriculture, as well as analysis of debris field after natural disasters. We show that deep learning can be effectively applied on products from SfM, which may have artifacts resulting from reconstruction, or spurious features from prior network training. The presented system has advantages of low-cost, rapid deployment and analysis, statistically accurate results, high generalization to other fields, and automated processing with limited expert intervention. In comparison with deep learning methods on plain UAS imagery [3, 4], the UAS-SfM-DL paradigm has various advantages. First, it can produce consistent georeferenced semantic maps, enabling large-scale precise spatial

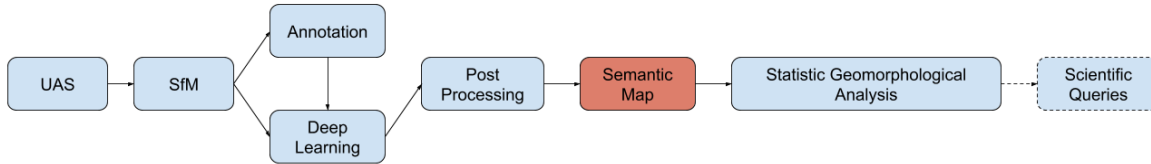


Fig. 2. The workflow of UAS-SfM-DL. The presented method is straightforward to implement. It expands the utility of the models from UAS-SfM. UAS-SfM-DL can provide semantic geomorphological maps with georeferenced instance segmentation, which enables spatial distribution analysis.

analysis. Second, orthomosaics acquired through SfMs can potentially result in rich high-resolution imagery of very large sites. When applying deep neural networks on large orthomosaics, the model size increases significantly. Instead of relying on expensive compute, we propose an affordable solution that trains and infers on small tiles split from a large map. We present a registration algorithm to merge semantic objects from multiple tiles during inference. This UAS-SfM-DL system was used to analyze rock traits along a tectonic fault scarp in Bishop, California (Fig. 1).

Rock traits such as size, shape, orientation, and composition, are of importance in earthquake geology research. Rock size (major-axis length) distributions reflect both the initial cooling joint fracture geometry, as well as faulting-induced fracturing and vary with position as a function of strain magnitude and linkage characteristics. Rock orientations indicate the degree of downslope transport along the fault scarps, enhancing our understanding of the fault scarp erosional processes and providing future insight on precariously balanced rocks (PBR) toppling reconstruction. We apply our UAS-SfM-DL pipeline to isolate desired rock traits within active fault zones. Our results show that deep neural networks trained on expert rock annotations on UAS-SfM orthomosaic generated for a geological site, leads to accurate and fast estimation of spatial distributions of rock traits. The deep neural network, once trained, significantly reduces manual efforts that typically coincide with large volumes of data.

## II. RELATED WORK

### A. Unpiloted Aircraft Systems and Structure from Motion (UAS-SfM)

Structure from motion originated in the computer vision community [5, 6], and has even enabled reconstruction from community photo collections [7]. With the recent availability of low cost UAS as well as software such as Agisoft and Pix4D [8, 9], UAS-SfM have widely been used in physical geography [10, 11, 12] in zones ranging from coastal environments [12], Antarctic moss beds [13], to fault scarps [14]. However, geomorphological analysis of products from UAS-SfM still depends a lot on geometric models carefully designed by experts [15, 16]. Our work presents a automatic approach for statistical analysis of geomorphic features, generalizable to other domains.

### B. Deep Learning in Close-range Aerial Imagery Processing

Deep learning has demonstrated unprecedented results in image classification [17], object detection [18], pixel segmentation [19], and object segmentation [20]. The advances in computer vision have facilitated the development of visual perception models deployed aboard UAS as well as ground vehicles in various applications like wildfire classification [21], weed classification [4], car detection [3], and fruit counting [22]. However, previous work largely targets raw camera imagery as the input to the deep learning models. Although tracking algorithms [23, 24] can reconstruct the objects of interest, they lack ground control points to globally correct geographic distortions, a step essential in geological and surveying applications.

Transitioning from 2D to 3D, deep learning has also been used to process the information from LiDAR point clouds. Point cloud data generated from trees was fed to fully connected layers to classify tree types [25]. PointNet [26], designed to process point cloud data, was applied to classify urban objects [27]. 3D convolution neural networks have been used to segment point clouds from TLS [28]. Our proposed work is limited to 2D analysis, however, we are exploring 3D neural networks to extend our work to 3D analysis of rocks.

### C. Deep Learning in Satellite Based Remote Sensing

The deep learning research for satellite image processing has been one of the most active areas in remote sensing [29, 30]. Applications of deep learning in remote sensing range from scene classification [31, 32], object detection [33, 34], and segmentation [35]. Apart from RGB images, deep learning has also been used on multi-spectral images [36, 37]. Unsupervised learning plays an important role in feature learning from satellite images [38, 39]. Super-resolution neural networks trained on available high-resolution ground truth have been used to enhance the resolution of satellite imagery [40, 41, 42]. However, resolution-enhanced satellite imagery cannot provide consistent and precise features needed for geological studies, as there may be artifacts from features learned on other sites. Additionally, due to the imagery resolution, current deep learning research for satellite imagery analysis is limited to large-scale objects and features [31, 43].

## III. SYSTEM DESCRIPTION

The workflow of our UAS-SfM-DL methodology is shown in Fig. 2. Aerial imagery from an UAS along with in-

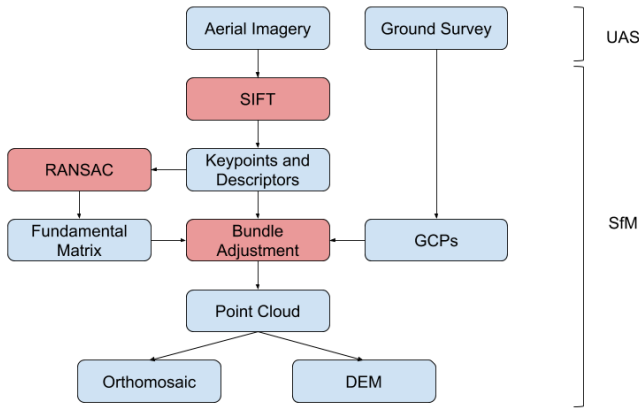


Fig. 3. UAS-SfM. Aerial imagery is taken from UAV surveys and then processed by SfM algorithms. Ground control points are collected with precise GPS coordinates measuring equipment and provided to SfM algorithms to scale the 3D reconstruction and improve the mapping accuracy.

formation of ground control points, are processed using SfM algorithms to reconstruct a site of study with high-resolution. Geologists annotate features of interest such as rock boundaries for a portion of the high-resolution orthomosaic. Deep neural networks are trained on this annotated imagery, and inference is carried out on unlabelled imagery from the whole site. Segmented objects inferred by the deep learning models are post-processed by geometric structural analysis and shape descriptors to estimate properties such as rock diameter and orientation. Semantic maps are produced by combining the semantic information from deep learning with post-processing. Statistical studies are carried out on the resulting semantic maps to estimate distribution of rock diameter and orientation.

#### A. UAS-SfM

Fig. 3 shows the details of the UAS-SfM sub-system. Key points in each aerial image are detected by SIFT algorithm [44], which is invariant to scale and rotation of features. SIFT assigns each keypoint a local descriptor, which is used to match correspondence between keypoints using approximate nearest neighbors for each pair of images. With the matched keypoints, and the RANSAC algorithm is used to estimate the fundamental matrix for each pair of images. The remaining matched keypoints are organized into tracks. Bundle adjustment is used to iteratively estimate camera parameters and tracked keypoint positions by minimizing the sum of the reprojection errors:

$$\sum_{c=1}^n \sum_{k=i}^m \delta_{c,k} \|q_{c,k} - \mathbf{P}(\Theta_c, p_k)\|$$

where  $\Theta_c$  is the parameters of the  $c$ -th camera. There are  $n$  cameras (or camera images) and  $m$  tracked keypoints. This parameter includes the 3D orientation (three parameters), the camera center (three parameters), and the focal length (one parameter). Parameter  $p_k$  is the position of the tracked  $k$ -th keypoint,  $\mathbf{P}$  is reprojection function that transforms keypoint

$p$  to homogeneous image coordinates by perspective projection, and  $q_{c,k}$  is the observed projection of the  $k$ -th keypoint on the  $c$ -th camera.  $\delta_{c,k}$  is an indicator variable where  $\delta_{c,k} = 1$  if the  $c$ -th camera observes the  $k$ -th keypoint, otherwise  $\delta_{c,k} = 0$ . To add precise metric scale to the reconstruction of keypoints and reduce global distortions, ground control points from ground survey such as GPS surveying instruments, are added to the bundle adjustment optimization as constraints. The primary product of SfM is point cloud from the tracked keypoints. Rastered orthomosaic is generated by interpolation and orthogonal projection.

The orthomosaic is formatted as a GeoTiff file whose meta data has information such as global coordinates, projection type, and ground resolution from which we can acquire the global coordinates of each pixel in the map. These high-resolution orthomosaics enable precise spatial analysis of semantic features from deep learning.

#### B. Deep Learning

We use deep neural networks to automatically extract semantic information from the georeferenced orthomosaics estimated using SfM. We use the RGB channels of the orthomosaic as the input to the neural network. The selection of neural network architecture depends on the features and distributions of objects of interest. Generally, segmentation neural networks such as U-Net [19] can be used when the goal is pixel-level segmentation. Region proposal networks such as Faster-RCNN [45] can detect individual objects with bounding boxes, though this information alone cannot produce major-axis length and orientation information required for geometric properties of objects such as rocks. We choose the Mask-RCNN deep neural network architecture for this study since it generates both bounding boxes as well as corresponding masks for object instances (rocks) [20]. Due to the densely-spatial distribution of rocks at a fault scarp, we select the Pyramid Feature Network (PFN) [46] as the backbone of the object detection network. PFN's multi-scale, pyramidal hierarchy of anchor generation mechanism is suitable for object detection in such a setting.

#### C. Tiling

The orthomosaic of survey sites produced by SfM is usually of high-resolution (for the fault scarp, 25664x10589). Directly working with high-resolution images for neural network training or inference is computationally challenging since it poses high demand on GPU RAM. To address this limitation, we split the orthomosaic into smaller tiles (400x400 pixels) without overlap for training. We randomly choose a subset of tiles and annotate rocks using polygons in LabelMe [47] as the shape primitive. 90% of image tiles are used for training and the remaining 10% for testing. We augment the training dataset 400 fold by the combination of random left-right flipping, top-down flipping, rotation, and zooming-in (cropping) and zooming-out.

Once the network has been trained, to detect objects at the edges of tiles and merge them if they are from one instance, we develop a registration scheme. Fig. 5 shows the



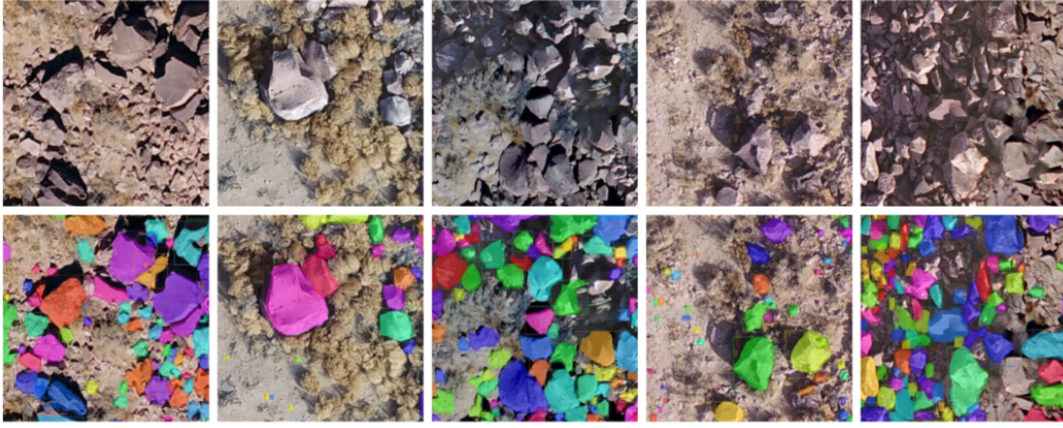


Fig. 4. Prediction of Mask RCNN on test dataset. Colors are randomly selected to distinguish rocks.

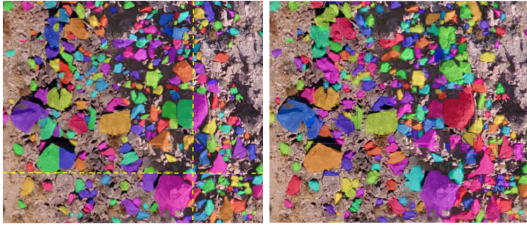


Fig. 5. Rock registration at boundaries. Left) the rocks at the edges of each inference are not merged; right) any two rocks at the edges of each inference are merged and registered as one if they belong to same instance.

problem caused by splitting orthomosaic and the results by our registration algorithm (Algorithm 1). When carrying out inference, we split the orthomosaic into 400x400 pixel tiles with 10-pixel overlap on height and width. Then we check if two georeferenced rock instances on each 10-pixel region of overlap between two adjacent tiles have a overlap above a certain threshold (20 pixels). If true, the two rock instances are merged and registered as one instance. Fig. 5 illustrates the result of this operation on a representative tile pair.

#### D. Post Processing

Post processing is necessary to compensate for errors that result from the data-driven nature of neural networks, and to identify the rocks on the fault scarp. The segmentation sub-network has stochastic errors, with one example shown in Fig. 7 (left) wherein a hole is present in the segmented rock body. We assume that there are no rocks with torus topology on the fault scarp, and use topological structure analysis to remove such artifacts [48]. The contours of rocks are generated, with the largest contours retained as the outlines of the rocks. The rocks sizes are approximated by the number of pixels in the largest contours. Note that georeferenced models enable to associate rock size in pixels and rock size in meters, which is more accurate than the association from plain 2D camera photos.

Since the fault scarp has a steep slope, we first estimate gradient of the DEM [49], then denoise it with Gaussian filtering. From the smoothed slope map, the fault scarp is

---

#### Algorithm 1 Rock Registration

---

**input:** orthomosaic, neural\_network

**output:** registered\_rocks

---

```

1. tiles = overlap_split(orthomosaic)
2. rocks = project(neural_network(tiles))
3. registered_rock = None
4. for rock in rocks:
    if rock.bb is on its own overlaps:
        id = check_bb_overlap(rock.bb, registered_rocks)
    if id ≠ None:
        if check_IOU(rock.mask, registered_rocks[id].mask)
           > threshold:
            merge(registered_rocks[id], rock)
        continue
    register(registered_rocks, rock)

```

---

Comments:

**overlap\_split:** splits orthomosaic into 400x400-pixel tiles with 10-pixel horizontal and vertical overlaps

**project:** projects local bounding boxes with pixel coordinates to global coordinates

**check\_bb\_overlap:** returns None if there is no registered rocks having bounding box overlap with the rock, otherwise returns its id

**check\_IOU:** returns the intersection of union of two masks

**merge:** merges the bounding boxes and masks to the registered rock

**register:** registers new rock

---

identified by the slope above a certain threshold and further smoothed through morphological transformations such as opening, dilation, erosion, and etc.

## IV. RESULTS

In this section, we discuss the results of our pipeline on the imagery acquired on the rock scarp. We conducted surveys of the Volcanic Tablelands with a DJI Phantom 4 Pro, implementing a grid flight pattern with 66% image overlap, and a 90° (straight down) camera angle. The Volcanic Tablelands is a faulted plateau over the approximately 150m thick welded Bishop Tuff (760 ka) at the north end of Owens Valley near Bishop, CA. The flight altitude was between 70 – 100 meters above ground level (the height of fault scarp slope is about 30 meters). Flights were carried out at an altitude of 70 – 100 meters above ground level, with a 20 Megapixel onboard camera collecting images at a resolution of 5472x3648. The field of view of the camera is 84°, resulting in effective spatial resolution of 3cm /pixel. While



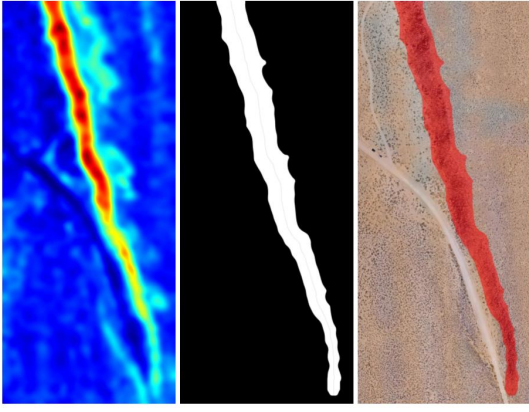


Fig. 6. Identifying fault scarp. Left) slope map; right) fault scarp contour with skeleton

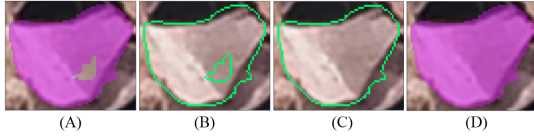


Fig. 7. Contour analysis to compensate instability of segmentation prediction. (A) mask prediction from Mask RCNN; (B) contours by topological structure analysis; (C) the largest contour kept to approximate outline of the rock; (D) filtered mask

we used RGB bands for the experiment, SfM is not limited to dealing with visible bands, and in our recent results, we have obtained multispectral orthomosaics as well.

The 25664x10589 orthomosaic was split into 400x400 tiles using Python GDAL tools. 51 tiles were annotated by human experts. 45 tiles were used for training, and 6 for testing. The neural network was initialized with well trained weights from COCO 2017 and then retrained on one NVIDIA RTX 2080 Ti for 15 hours by stochastic gradient optimization with an initial learning rate 0.001, learning momentum 0.9, and weight decay 0.0001. The performance of the network is shown in Table I.

Fig. 4 shows the inference results on images from the test dataset, which are not exposed to the training processes. We studied the effect of data augmentation on generalization of neural network models. After training the network on the augmented training dataset and non-augmented training dataset, we measured the performance on the test dataset (Table I). We found that training augmented dataset with batch normalization [50] improved the mean recalls  $mR_{50}$  by 65% on the test dataset.

To remove outliers on the perimeter, we decided the fault scarp from the slope map. Fig. 6 shows the slope map

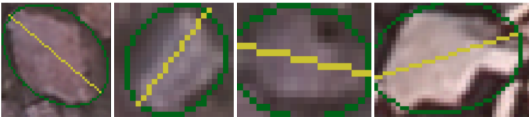


Fig. 8. Ellipse fitting and estimation of major orientations from the inferred rock boundaries.

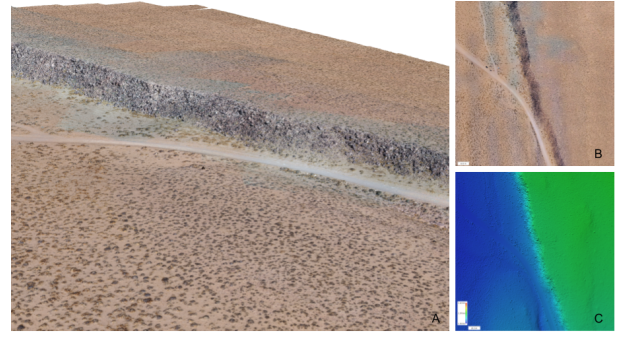


Fig. 9. Results of SfM. (A) 3D point cloud; (B) orthomosaic; (C) DEM. The ground sample distance of orthomosaic is 0.019m/pixel. The ground sample distance of DEM is 0.079m/pixel.

TABLE I  
TRAINING RESULTS ON TEST DATASET

	Mack RCNN w. BN		Mask RCNN w.o. BN	
	aug train	non-aug train	aug train	non-aug train
$mAP_{50}$	0.56	0.42	0.55	0.40
$mR_{50}$	0.36	0.34	0.26	0.20

We measured mean average precision and mean recall on test dataset with and without batch normalization during training.

and the fault scarp contour. The rock were estimated by the refined masks from topological structure analysis. We explored methods of visualizing individual rocks, and a straightforward approach is to load the georeferenced Tiff image in Google Earth. Fig. 10 (D) shows the results of the filtered rock instances superimposed on the fault scarp digital surface model as color masks, in Google Earth. Finally, we used the georeferenced rock boundary information to estimate rock diameter and orientation distribution. To approximate major orientations of rocks, we fit the refined masks with ellipses [51] as shown in Fig. 8. The orientations of rocks are parameterized by eccentricity and an angle describing the major axes of the ellipse. Fig. 11 (D) shows the polar histogram of major orientations.

Apart from the rock traits distributions on the entire fault scarp, the distributions along the cross strike of the fault scarp, which is the direction perpendicular to the fault scarp (Fig. 12), is also of interest. We computed the skeleton of the fault scarp contour to acquire the middle spline [52]. We selected a subsection of the middle spline and approximate it with a straight line by linear regression. We consider the normal vector of the straight line as the cross strike direction. We drew 9 boxes along the cross strike direction at the two sides of the middle line and represent rock size distributions in the boxes by the normalized rock size histograms.

Detailed rock diameter histogram for the scarp is shown in Fig. 12. The whole fault scarp is divided to 16 areas. Each area is divided to nine boxes along the cross strike. In each box as the inlay, there are 20 bins representing different rock diameter histogram in the true area. From the bottom to top in each area, the rock diameter uniformly varies from 0 to 3.6 meters. The small opaque boxes at the left side of the transparent areas show the histogram. The mean rock

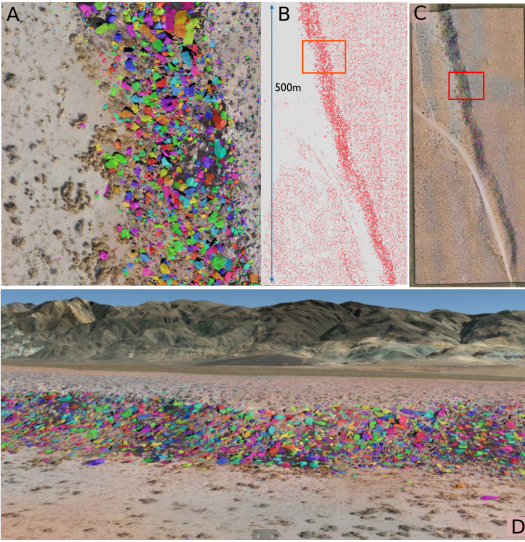


Fig. 10. Color segmentation visualization. (A) Partial enlargement of the red box in B and C; (B) Polygons of  $\sim 80,000$  rocks from the site including outliers; (C) Segmentation on the area of study; (D) Ground view after importing in Google Earth

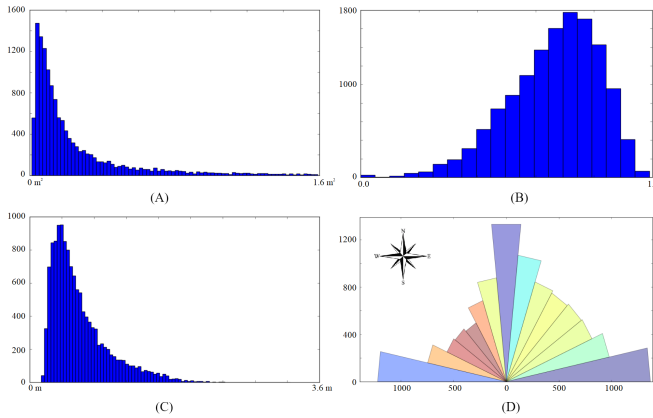


Fig. 11. Rock size histograms and major orientation histogram. (A) the rock size histogram on the fault scarp. The rock sizes are approximated by the pixel numbers in the refined masks. The horizontal axis is rock area in  $meter^2$ , and the vertical axis is the number of rocks. (B) the rock eccentricity histogram on the fault scarp. (C) the rock major length histogram on the fault scarp. The major length is  $L = 2a$ , where  $a$  is the semimajor axis of the fitting ellipse  $\frac{x^2}{a^2} + \frac{y^2}{b^2} = 1$ . (D) the polar histogram of major orientation on the fault scarp.

diameter for each box, is shown in the heatmap along the scarp.

## V. CONCLUSIONS

In this paper, we presented a pipeline for geomorphological analysis using structure from motion and deep learning on close-range aerial imagery. Our UAS-SfM-DL methodology was used to estimate distribution of rock traits (diameter and orientation) on a fault scarp in the Volcanic Tablelands, California. In future, we will study the correlations between rock trait distributions and fault scarp slip rate. Our current pipeline is limited to 2D representations of rocks. Naturally, a key next step is to explore 3D rock trait analysis. To

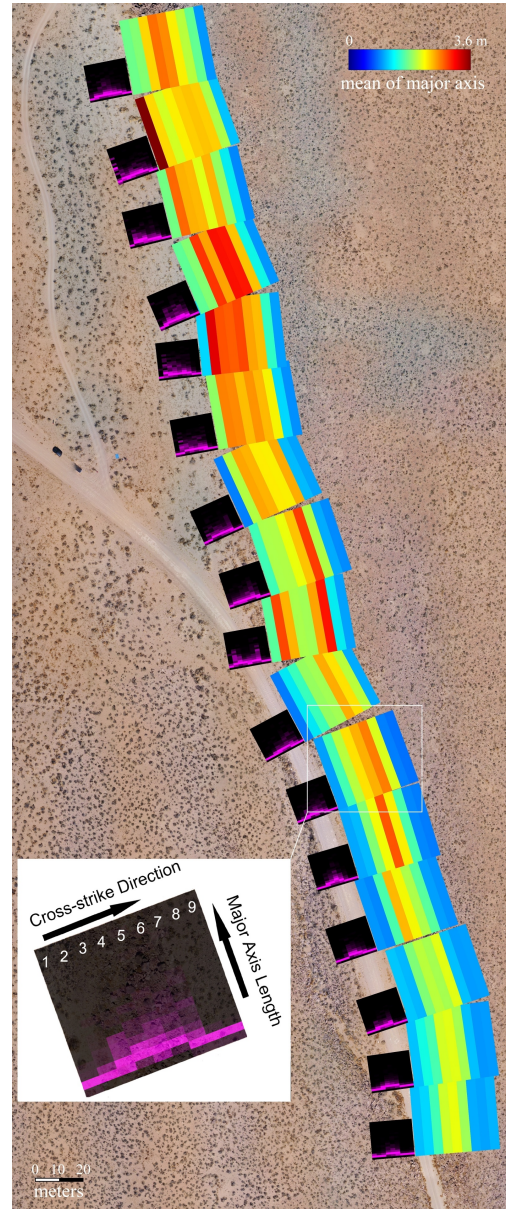


Fig. 12. Detailed rock diameter (major-axis length) heatmap for the study area. Each area on the fault scarp is divided into nine boxes along cross strike. The heatmap on the fault scarp shows the mean rock diameter for each box along the scarp. The smaller black plots show the detailed histogram of rock diameters, instead of just the mean diameter shown in the heatmap.

do so, we are working on localizing the rocks in the 3D point cloud to estimate surface models of individual rocks, enabling estimation of properties such as stability of precariously balanced rocks. To improve 3D segmentation, we will explore neural networks that process point-cloud and RGB-D data directly.

## ACKNOWLEDGEMENTS

This work was supported in part by Southern California Earthquake Center (SCEC) award 19179, and National Science Foundation award CNS-1521617.

## REFERENCES

- [1] Michael F Goodchild. “Twenty years of progress: GIScience in 2010”. In: *Journal of spatial information science* 2010.1 (2010), pp. 3–20.
- [2] J Barrett Salisbury et al. “Validation of meter-scale surface faulting offset measurements from high-resolution topographic data”. In: *Geosphere* 11.6 (2015), pp. 1884–1901.
- [3] Nassim Ammour et al. “Deep learning approach for car detection in UAV imagery”. In: *Remote Sensing* 9.4 (2017), p. 312.
- [4] Calvin Hung, Zhe Xu, and Salah Sukkarieh. “Feature learning based approach for weed classification using high resolution aerial images from a digital camera mounted on a UAV”. In: *Remote Sensing* 6.12 (2014), pp. 12037–12054.
- [5] Minas Spetsakis and John Yiannis Aloimonos. “A multi-frame approach to visual motion perception”. In: *International Journal of Computer Vision* 6.3 (1991), pp. 245–255.
- [6] Carlo Tomasi and Takeo Kanade. “Shape and motion from image streams under orthography: a factorization method”. In: *International Journal of Computer Vision* 9.2 (1992), pp. 137–154.
- [7] Noah Snavely et al. “Scene reconstruction and visualization from community photo collections”. In: *Proceedings of the IEEE* 98.8 (2010), pp. 1370–1390.
- [8] Agisoft Photoscan. <https://www.agisoft.com/>. 2018.
- [9] Pix4D. <https://www.pix4d.com/>. 2019.
- [10] Matthew J Westoby et al. “‘Structure-from-Motion’ photogrammetry: A low-cost, effective tool for geoscience applications”. In: *Geomorphology* 179 (2012), pp. 300–314.
- [11] MW Smith, JL Carrivick, and DJ Quincey. “Structure from motion photogrammetry in physical geography”. In: *Progress in Physical Geography* 40.2 (2016), pp. 247–275.
- [12] Francesco Mancini et al. “Using unmanned aerial vehicles (UAV) for high-resolution reconstruction of topography: The structure from motion approach on coastal environments”. In: *Remote Sensing* 5.12 (2013), pp. 6880–6898.
- [13] A Lucieer, Sharon A Robinson, and D Turner. “Unmanned aerial vehicle (UAV) remote sensing for hyperspatial terrain mapping of Antarctic moss beds based on structure from motion (SfM) point clouds”. In: (2011).
- [14] Andrea Donnellan et al. “Geodetic Imaging of Fault Systems from Airborne Platforms: UAVSAR and Structure from Motion”. In: *IGARSS 2018-2018 IEEE International Geoscience and Remote Sensing Symposium*. IEEE. 2018, pp. 7878–7881.
- [15] Kristen L Cook. “An evaluation of the effectiveness of low-cost UAVs and structure from motion for geomorphic change detection”. In: *Geomorphology* 278 (2017), pp. 195–208.
- [16] MP Bunds et al. “Three Dimensional Aseismic Creep Deformation from Differencing of Structure from Motion and LiDAR High Resolution Topography on the San Andreas Fault, California”. In: *AGU Fall Meeting Abstracts*. 2018.
- [17] Kaiming He et al. “Deep residual learning for image recognition”. In: *Proceedings of the IEEE conference on computer vision and pattern recognition*. 2016, pp. 770–778.
- [18] Ross Girshick. “Fast r-cnn”. In: *Proceedings of the IEEE international conference on computer vision*. 2015, pp. 1440–1448.
- [19] Olaf Ronneberger, Philipp Fischer, and Thomas Brox. “U-net: Convolutional networks for biomedical image segmentation”. In: *International Conference on Medical image computing and computer-assisted intervention*. Springer. 2015, pp. 234–241.
- [20] Kaiming He et al. “Mask r-cnn”. In: *Proceedings of the IEEE international conference on computer vision*. 2017, pp. 2961–2969.
- [21] Yi Zhao et al. “Saliency detection and deep learning-based wildfire identification in UAV imagery”. In: *Sensors* 18.3 (2018), p. 712.
- [22] Steven W Chen et al. “Counting apples and oranges with deep learning: A data-driven approach”. In: *IEEE Robotics and Automation Letters* 2.2 (2017), pp. 781–788.
- [23] Xu Liu et al. “Robust fruit counting: Combining deep learning, tracking, and structure from motion”. In: *2018 IEEE/RSJ International Conference on Intelligent Robots and Systems (IROS)*. IEEE. 2018, pp. 1045–1052.
- [24] Xu Liu et al. “Monocular Camera Based Fruit Counting and Mapping with Semantic Data Association”. In: *IEEE Robotics and Automation Letters* (2019).
- [25] Haiyan Guan et al. “Deep learning-based tree classification using mobile LiDAR data”. In: *Remote Sensing Letters* 6.11 (2015), pp. 864–873.
- [26] Charles R Qi et al. “Pointnet: Deep learning on point sets for 3d classification and segmentation”. In: *Proceedings of the IEEE Conference on Computer Vision and Pattern Recognition*. 2017, pp. 652–660.
- [27] Younes Zegaoui et al. “Urban object classification with 3D Deep-Learning”. In: *JURSE: Joint Urban Remote Sensing Event*. 2019.
- [28] Zhou Guo and Chen-Chieh Feng. “Using multi-scale and hierarchical deep convolutional features for 3D semantic classification of TLS point clouds”. In: *International Journal of Geographical Information Science* (2018), pp. 1–20.
- [29] Liangpei Zhang, Lefei Zhang, and Bo Du. “Deep learning for remote sensing data: A technical tutorial on the state of the art”. In: *IEEE Geoscience and Remote Sensing Magazine* 4.2 (2016), pp. 22–40.



- [30] Xiao Xiang Zhu et al. "Deep learning in remote sensing: A comprehensive review and list of resources". In: *IEEE Geoscience and Remote Sensing Magazine* 5.4 (2017), pp. 8–36.
- [31] Qin Zou et al. "Deep learning based feature selection for remote sensing scene classification". In: *IEEE Geoscience and Remote Sensing Letters* 12.11 (2015), pp. 2321–2325.
- [32] Nataliia Kussul et al. "Deep learning classification of land cover and crop types using remote sensing data". In: *IEEE Geoscience and Remote Sensing Letters* 14.5 (2017), pp. 778–782.
- [33] Xueyun Chen et al. "Vehicle detection in satellite images by hybrid deep convolutional neural networks". In: *IEEE Geoscience and remote sensing letters* 11.10 (2014), pp. 1797–1801.
- [34] Tianwen Zhang and Xiaoling Zhang. "High-Speed Ship Detection in SAR Images Based on a Grid Convolutional Neural Network". In: *Remote Sensing* 11.10 (2019), p. 1206.
- [35] Michael Kampffmeyer, Arnt-Borre Salberg, and Robert Jenssen. "Semantic segmentation of small objects and modeling of uncertainty in urban remote sensing images using deep convolutional neural networks". In: *Proceedings of the IEEE conference on computer vision and pattern recognition workshops*. 2016, pp. 1–9.
- [36] Maria Vakalopoulou et al. "Building detection in very high resolution multispectral data with deep learning features". In: *2015 IEEE International Geoscience and Remote Sensing Symposium (IGARSS)*. IEEE. 2015, pp. 1873–1876.
- [37] Hannah R Kerner et al. "Novelty Detection for Multispectral Images with Application to Planetary Exploration". In: *Proceedings of the AAAI Conference on Artificial Intelligence*. Vol. 33. 2019, pp. 9484–9491.
- [38] Adriana Romero, Carlo Gatta, and Gustau Camps-Valls. "Unsupervised deep feature extraction for remote sensing image classification". In: *IEEE Transactions on Geoscience and Remote Sensing* 54.3 (2015), pp. 1349–1362.
- [39] Qian Shi, Xiaoping Liu, and Xia Li. "Road detection from remote sensing images by generative adversarial networks". In: *IEEE access* 6 (2018), pp. 25486–25494.
- [40] Kui Jiang et al. "Deep distillation recursive network for remote sensing imagery super-resolution". In: *Remote Sensing* 10.11 (2018), p. 1700.
- [41] Jonathan Chin and Asif Mehmood. "Generative adversarial networks based super resolution of satellite aircraft imagery". In: *Pattern Recognition and Tracking XXX*. Vol. 10995. International Society for Optics and Photonics. 2019, 109950W.
- [42] Ying Tai, Jian Yang, and Xiaoming Liu. "Image super-resolution via deep recursive residual network". In: *Proceedings of the IEEE conference on computer vision and pattern recognition*. 2017, pp. 3147–3155.
- [43] Min Ji et al. "A Comparative Study of Texture and Convolutional Neural Network Features for Detecting Collapsed Buildings After Earthquakes Using Pre- and Post-Event Satellite Imagery". In: *Remote Sensing* 11.10 (2019), p. 1202.
- [44] David G Lowe. "Distinctive image features from scale-invariant keypoints". In: *International journal of computer vision* 60.2 (2004), pp. 91–110.
- [45] Shaoqing Ren et al. "Faster r-cnn: Towards real-time object detection with region proposal networks". In: *Advances in neural information processing systems*. 2015, pp. 91–99.
- [46] Tsung-Yi Lin et al. "Feature pyramid networks for object detection". In: *Proceedings of the IEEE Conference on Computer Vision and Pattern Recognition*. 2017, pp. 2117–2125.
- [47] Bryan C Russell et al. "LabelMe: a database and web-based tool for image annotation". In: *International journal of computer vision* 77.1-3 (2008), pp. 157–173.
- [48] Satoshi Suzuki et al. "Topological structural analysis of digitized binary images by border following". In: *Computer vision, graphics, and image processing* 30.1 (1985), pp. 32–46.
- [49] Berthold KP Horn. "Hill shading and the reflectance map". In: *Proceedings of the IEEE* 69.1 (1981), pp. 14–47.
- [50] Sergey Ioffe and Christian Szegedy. "Batch normalization: Accelerating deep network training by reducing internal covariate shift". In: *arXiv preprint arXiv:1502.03167* (2015).
- [51] Andrew W Fitzgibbon, Robert B Fisher, et al. *A buyer's guide to conic fitting*. University of Edinburgh, Department of Artificial Intelligence, 1996.
- [52] TY Zhang and Ching Y Suen. "A fast parallel algorithm for thinning digital patterns". In: *Communications of the ACM* 27.3 (1984), pp. 236–239.